Structural Engineering and Mechanics, Vol. 37, No. 1 (2011) 1-15
DOI: http://dx.doi.org/10.12989/sem.2011.37.1.001

Elucidating the mechanical behavior of ultra-high-strength concrete under repeated impact loading

Yuh-Shiou Tai* and Iau-Teh Wang

Department of Civil Engineering, ROC Military Academy, 1 Weiwu Rd, Fengshan, 830, Taiwan, ROC

(Received August 9, 2009, Accepted September 7, 2010)

Abstract. The response of concrete to transient dynamic loading has received extensive attention for both civil and military applications. Accordingly, thoroughly understanding the response and failure modes of concrete subjected to impact or explosive loading is vital to the protection provided by fortifications. Reactive powder concrete (RPC), as developed by Richard and Cheyrezy (1995) in recent years, is a unique mixture that is cured such that it has an ultra-high compressive strength. In this work, the concrete cylinders with different steel fiber volume fractions were subjected to repeated impact loading by a split Hopkinson Pressure Bar (SHPB) device. Experimental results indicate that the ability of repeated impact resistance of ultra-high-strength concrete was markedly superior to that of other specimens. Additionally, the rate of damage was decelerated and the energy absorption of ultra-high-strength concrete improved as the steel fiber volume fraction increased.

Keywords: steel fiber reinforced concrete; repeated impact; Hopkinson Pressure Bar test.

1. Introduction

Concrete is the most commonly used construction material worldwide, which, during its working process, is frequently subjected to quasi-static loadings of magnitudes that change slowly. Designs of such large structures as nuclear power plant protection devices, airport runways and military facilities must however account for the impact of dynamic loadings of drastically changing magnitudes. Consequently, the materials chosen must resist shock and penetration and have high capacity for energy absorption. Concrete is typically comprised of cement, aggregate, water and an additive mixed according to a fixed ratio. As common concrete is known for its high compressive strength and low tensile strength, it is typically employed for its compressive strength, while the tensile strength is achieved by the use of steel bars. Whether a reinforced concrete component can be used effectively is largely dependent on whether concrete and steel bar deformation can be effectively transferred. Under quasi-static loadings, this criterion can be satisfied. However, under dynamic or shock loading, this criterion cannot be satisfied easily, mainly because such loading is generally local and stress is transmitted within the material as stress waves, which generate reflection within the concrete and at the interface where compressive waves become tensile waves. The fact determining the stress distribution inside reinforced concrete is difficult complicates the

*Corresponding author, Ph.D., E-mail: ystai@cc.cma.edu.tw

design process. The conventional design approach uses a high concentration of steel bars at various locations in the concrete, which increases cost and construction difficulty. For improving this property, high-strength fiber reinforced concrete was developed. The high-strength concrete (HSC), which is designed to have a strength under compression of over 41 MPa (ACI 1984) is extensively employed (Smadi and Belakhdar 2007, Zhang *et al.* 2009). The compressive strength of concrete can be increased by increasing the strength of the cement paste and improving the interfacial zone, reducing the potential stress concentration between the aggregate and the cement paste. Such an increase can be achieved by reducing the water-to-cement ratio, using fine pozzolanic materials and reducing the coarse aggregate size. Based on current knowledge, concrete with a 28 day ultra-high compressive strength of 150 MPa can be made easily.

Fibers suitable for reinforcing concretes can be made of steel, glass and organic polymers. In particular, the steel fiber-reinforced concrete possesses many excellent dynamic performances such as high resistance to explosion and penetration, as compared to plain concrete and even the traditionally reinforced concrete in civil engineering. The application of steel-fiber concrete, therefore, has garnered the attention of researchers (Banthia *et al.* 1996, Bindiganavile and Banthia 2005, Banthia *et al.* 1998, Wang *et al.* 2008). Findings also indicate that SFRC is a better energy absorbing and impact resisting material. In addition to typical civilian and infrastructure projects, steel-fiber concrete has shown great promise for securing military structures. A notable example is (SIFCON), which was developed by (Lankard 1985). When creating SIFCON, flowing mortar is injected into a steel fiber skeleton situated in the false work. High-strength steel-fiber concrete contains 5-20% of steel fibers in mass. Experimental results indicate that SIFCON, due to the large amount of steel fibers, has significantly enhanced compressive and tensile strength. Especially noteworthy is that its toughness and ability to absorb energy are about 60 times greater that those of conventional concrete. (Hackman *et al.* 1992) studied (SIMCON), the basic materials and construction process of which is similar to those of SIFCON. The major difference between SIMCON and SIFCON is that the steel fiber net in SIMCON is formed by profiling molten iron and placing it in layers. The thickness of the steel fiber net is typically 13-50 mm. Experiment results demonstrate that when the volume fractions of steel fibers in SIMCON is 12% of that in SIFCON, bending strength can reach 50% of that of SIFCON. Reducing the amount of steel fibers significantly reduces cost. (Richard and Cheyrezy 1995) developed Reactive Powder Concrete (RPC), and divided RPC into RPC200 and RPC800 based on strength. The enhanced strength of RPC is achieved by an improved mixing technique and treatment method that markedly increase the compression strength of concrete by 170-230 MPa. After adding steel aggregate and applying a pressure of 50 MPa before solidification, the strength of RPC800 can be as high as 800 MPa. Although the special technical requirements make its application increasingly challenging, it has opened a door for new concrete research.

Reinforcement using steel fibers can improve the fracture toughness, compressive strength and the durability of the reinforced concrete structures (Teng *et al.* 2004, Deng and Li 2007). However, the energy absorption of ultra-high-strength concrete is rarely explored so far in the open literature. In this study, the impact compression experiment is described in detail, including the fabrication of ultra-high-strength concrete specimen with different steel-fiber volume fractions. The split Hopkinson Pressure Bar (SHPB) test was extended for repeated impact testing and examining the dynamic responses of different specimens under repeated impact, including fracture mode, during which damage accumulates. Results of this study provide a valuable reference for the research and design of concrete.

2. Experimental program

2.1 Materials

Cement used in this study was ordinary Portland cement which conforms to ASTM Type II. This is medium sulfate-resisting cement with low calcium aluminates C_3A content. Dry non-compacted silica fume was used as mineral additive; it has a silicon dioxide content of 90%, specific gravity of 2.2, and a specific surface of 18~20 m^2/g. The chemical compositions of the cement and SF are shown in Table 1.

The coarse aggregate was natural crushed gravel of continuous grades with a maximum particle size of 10 mm, a specific gravity of 2.65, and absorption% of 1.3%. The coarse aggregate is washed and left to be air dried to saturated surface dry condition before being used. Two types of sand were used in the study; natural sand with a maximum particle size of 4.7 mm and a fineness modulus of 2.41, and quartz sand with a maximum particle size of 0.6 mm. Crushed crystalline quartz powder is a critical component in heat-treated RPC concretes. The reactivity during heat treatment is maximal for an average particle size of between 5~25 μm. An average particle size of 10 μm was used. To improve slurry at low water-cement ratios, a high-performance water-reducing agent was used in the study. The chemical ingredient in the agent that is acrylic graft polymer anionic high molecular surfactant, it complies with ASTM C 494 Types G. The admixture is light-brown in color, with a specific gravity of 1.07~1.13. Waved steel fibers were made from cold drawn low-carbon

Table 1 Properties of cement and silica fume

Material	Cement	SF
Chemical composition (%)		
SiO_2	22.60	90
Al_2O_3	3.75	1
Fe_2O_3	4.55	1
CaO	63.15	0.4
MgO	2.17	1
SO_3	1.88	
C		2
Loss on ignition, L.O.I	0.62	3

Table 2 Concrete mix proportions (kg/m^3)

Specimen No.	*w/(c+sf)*	Cement	Water	Silica fume	Coarse aggregate	Natural sand	Quartz sand	Quartz powder	Steel fiber	Superplasticizer
HSC-F1	0.2	675	150	75	971	514	---	---	80	21
HSC-F2	0.2	675	150	75	944	514	---	---	160	30
UHSC-F1	0.2	750	185	179	---	---	969	189	80	40
UHSC-F2	0.2	750	185	179	---	---	942	189	160	40
UHSC-F3	0.2	750	185	179	---	---	916	189	240	40

steel. The fiber length was 12 mm and the diameter was 0.175 mm; therefore, the aspect ratio of the fibers (l/d) was 69. The details of the mix proportions are shown in Table 2.

2.2 Mixing proportions and specimen casting

Concrete mixes were prepared using a Hobart-type laboratory mixer with a capacity of 0.15 m^3. Cement, quartz fume, silica fume and silica sand were mixed first, and then water containing the appropriate amount of water-reducing agent was added. Steel fibers were added during the final mixing stage. The recommended dosages of the fibers by the manufacturer are divided into three categories, and the maximum dosage for each is 80, 160 and 240 kg/m^3. This corresponds to fiber volume fractions (V_f) of 1.0%, 2.0% and 3.0%, which is used in the study. One-third of the water-reducing agent was added during the final 3 min of mixing. Molds were oiled and placed on a vibration table vibrating at a low speed while the concrete was poured. After each mold was filled, vibration speed was increased to ensure good compaction. Following casting, specimens were covered with a plastic membrane to prevent moisture evaporation and were stored in the laboratory at 25°C for 24 h; samples were then de-molded and placed in a thermostat-controlled water tank at 90°C for curing for 96 h. Finally, specimens were removed and stored at room temperature until testing after 28 days.

2.3 Experimental steps

Prior to impact tests, this study performed a quasi-static compression test for each set of specimens. Quasi-static compressive tests were performed in a closed loop, servo-controlled MTS810 test machine with a capacity of 1000 kN (Fig. 1). Prior to testing, the ends of each

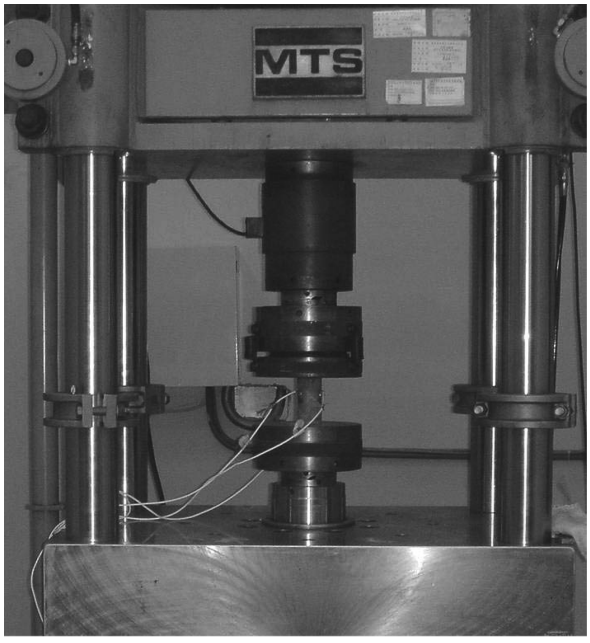

Fig. 1 Quasi-static test machine

specimen were ground until parallel. The stress-strain curves were plotted using a strain gauge with a gauge length of 30 mm; the gauge was attached to the test specimen to monitor axial deformations. During the experimental process, displacement was controlled and loading rates were 0.05 mm/min. Finally, maximum compressive strength and the stress-strain curve of each specimen were determined.

The concrete under impact load have been investigated since WWII and various test approaches have been developed. They include drop weight tests (Banthia *et al.* 1996, Bindiganavile and Banthia 2005, Banthia *et al.* 1998), pendulum-type tests, gas gun tests (Hanchak *et al.* 1992, Dancygier and Yankelevsky 1996, 1999, Zhang *et al.* 2005, Tai 2009) and split Hopkinson pressure bar tests (Tang *et al.* 1991, Ross *et al.* 1995, Wang *et al.* 2008). In this study, the SHPB test device for repeated impact tests was used, in which the elastic responses of different specimens under repeated dynamic loadings, as well as the fracture mode of accumulated damage, were examined. Specimens HSC-F1, HSC-F2, UHSC-F1, UHSC-F2 and UHSC-F3 were tested and assigned different codes (R-). For example, the response of specimen UHSC-F3 under the third impact is represented by UHSC-F1-R3. In the experiment, the gas pressure within the high-pressure steel bottle was controlled via a control system and pressure valve; thus, when the projectile was fired and hits the input bar during each test, the magnitude of the strain wave generated and action time remain identical. During repeated impacts, the number of impacts and strain signal of the elastic bar after each impact were recorded.

3. SHPB test principle

To study the mechanical properties of materials under dynamic loadings, the SHPB test device was used most frequently. Since it was first developed by Kolsky (1949), the SHPB device has been the primary method employed by researchers for dynamic testing, primarily because the SHPB device has the following characteristics. (1) The test process is simple. The stress-strain relationship of the specimen is determined via strain signals of the two elastic bars. Since one does not need to measure the signal from the specimen, specimen destruction does not affect data acquisition. (2) The loading wave form can be controlled easily. The characteristics of dynamic loading differ from those of static loading. The loading method affects; thus, the geometrical conditions and mechanical properties of a specimen influence test results. The SHPB device uses the input bar to measure the incident and reflection waves, the difference between which is the impact loading acting on a specimen. Furthermore, when a projectile slides along the barrel at speed V and hits the input bar, a stress impulse $\sigma_I(t)$ resembling a rectangle is generated in the input bar. The amplitude of this stress impulse ($= \rho CV/2$) can be controlled by adjusting impact velocity, V. Acting time is the time ($= 2L_B/C$) required for the projectile stress wave to travel back and forth once. Therefore, control can be achieved by adjusting the projectile length. In this manner, the strain rate of the specimen can be controlled and the stress-strain relationships under different strain rates explored.

3.1 Basic assumption

The SHPB experiment primarily utilizes one-dimensional wave propagation theory. During the experiment, both the input and output bars must remain elastic, the length-to-diameter ratio of the bars must be appropriate, and the following assumptions must be met (Kolsky 1949):

(1) Wave propagation in the bar meets the hypothesis of one-dimensional stress wave propagation theory.
(2) Stress-strain relationship of the specimen is evenly distributed longitudinally.
(3) Lateral inertial effect is ignored.

According to the theory of one-dimensional stress wave propagation, the expressions of stress, strain and strain rate of the specimen can be simplified as

$$\dot{\varepsilon}_S(t) = -\frac{2C}{l_S}\varepsilon_R \tag{1}$$

$$\varepsilon_S(t) = -\frac{2C}{l_S}\int_0^t \varepsilon_R dt \tag{2}$$

$$\sigma_S(t) = \frac{A}{A_0}E\varepsilon_T \tag{3}$$

where $C = \sqrt{E/\rho}$ is elastic wave velocity of the bar; E and p are the elastic modulus and mass density of the bar, respectively; ε_R is the reflected wave; ε_T is the transmitted wave; l_S is the specimen length; and A the cross-sectional area of the elastic bar. By using Eqs. (1)-(3) with the time parameter eliminated, one can obtain the dynamic stress-strain curve under a high strain rate.

According to the energy conservation principle, the energy absorption density of a specimen can be determined by calculating the change in input energy and output energy

$$E_s = \frac{1}{V_s}(E_I - E_R - E_T) \tag{4}$$

where V_s is specimen volume; E_I, E_R and E_T are incident energy, reflected energy and transmitted energy, respectively, which are expressed as

$$E_I = \frac{A}{\rho C}\int \sigma_I^2(t)dt \tag{5}$$

$$E_R = \frac{A}{\rho C}\int \sigma_R^2(t)dt \tag{6}$$

$$E_T = \frac{A}{\rho C}\int \sigma_T^2(t)dt \tag{7}$$

Fig. 2 shows the SHPB test device used in this experiment. The striker, incident pressure and transmitter bars are made of ANSI tool steel with a Young's modulus of 212.8 GPa. The striker, incident pressure and transmitter bars have identical diameters of 50 mm and lengths of 500.0, 1600.0 and 1600.0 mm, respectively. The end surfaces of the bars were lubricated to reduce friction. The axial impact of the striker bar and incident bar generates a compressive pulse, which is partially reflected when reaching the specimen between the incident bar and transmitter bar. The remaining portion of the wave is transmitted to the transmitter bar. The strain corresponding to the incident, reflected and transmitted pulses may then be measured using the strain gauge mounted on the bars connected via a Wheastone bridge. These signals, recorded by an oscilloscope and data-acquisition system, can be used to derive the corresponding strain pulses. For measuring the transient strain impulse, this study employs the strain gauge produced by KYOWA—gauge length is 5 mm,

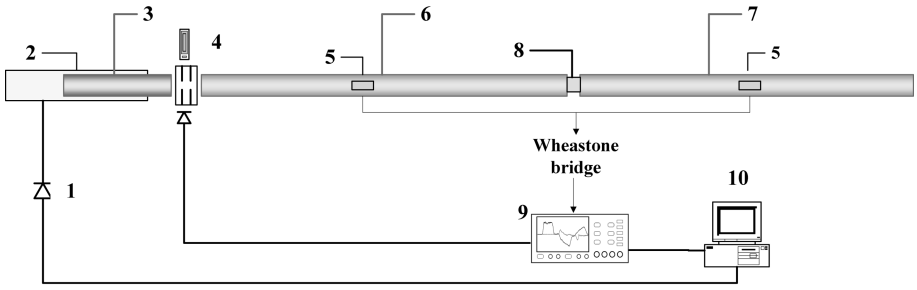

1: high-pressure air; 2: projectile guide barrel; 3: projectile; 4: grating velocity detection device; 5: strain gauge; 6: input bar; 7: output bar; 8: specimen; 9: signal amplifier and oscilloscope; 10: control box and data storage/analysis system

Fig. 2 A schematic of the split Hopkinson pressure bar apparatus

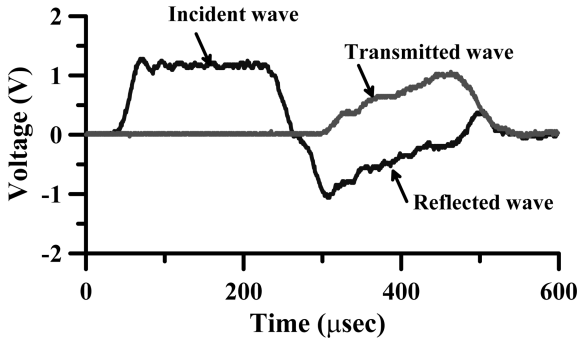

Fig. 3 Typical waves from the incident and transmitted bar

resistance is 120 Ω and signal rise time is roughly 0.89 μs. These properties are line with study requirements.

The oscilloscope in the SHPB impact test acquires the voltage signal. By rating the dynamic signal and the voltage-strain conversion via the calibrating voltage, one can determine the strain-time relationship of the incident wave, reflected wave and transmitted wave. Typical incident, reflected and transmitted waves corrected are shown in Fig. 3. Eqs. (1)-(3) yield the stress-strain curve and average strain rate.

3.2 Dispersion correction

The principal objective of dispersion correction is to transform strain gauge signals from the location of measurements back to the specimen-bar interface via a Fourier transform and dispersion equation. The method for dispersion correction—developed by Gong *et al.* (1990)—is summarized as follows.

(1) Determine the number of Fourier components to be used in the frequency domain.
(2) From a digitized time-domain pulse, determine the total number of points that represent the pulse to be analyzed. In the Fast Fourier Transform (FFT) numerical scheme, the total number of sample points should be a power of 2 to minimize numerical operations.
(3) Calculate phase velocity and wave speed, c_0.

(4) Derive the amplitude and phase angle of each Fourier component.
(5) Determine the phase angle difference due to wave propagation along a distance x
(6) Convert the signal back into the time domain to obtain the corrected pulse.

4. Results and discussion

4.1 Quasi-static test results

Fig. 4 shows the stress-strain curves of all specimens. When the steel-fiber volume fraction is 1%, the compressive strength of the HSC-F1 specimen is 109.5 MPa, and relative strain is 0.35%. When 2% steel-fiber is added, compressive strength of the HSC-F2 specimen is 101.9 MPa. For UHSC specimens, the compressive strengths are 139.7 MPa, 157.4 MPa and 190.1 MPa after adding 1%, 2% and 3% steel-fiber, respectively, and the stress and strain of maximum strength increase significantly. Table 3 lists the quasi-static mechanical testing results. It should be noted that UHSC

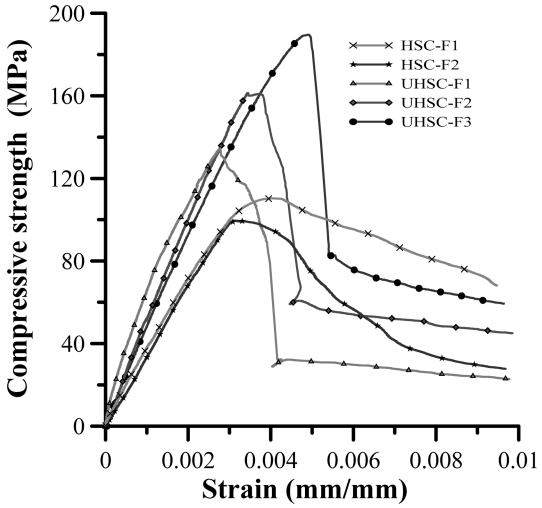

Fig. 4 Stress-strain curve of specimens HSC and UHSC

Table 3 Mechanical properties of HSC and UHSC

Specimen No.	Elastic Modulus (GPa)	Compression Strength (MPa)	Strain of Ultimate Strength (%)
HSC-F1	33.0	109.5	0.35
HSC-F2	33.9	101.9	0.29
UHSC-F1	48.5	139.7	0.26
UHSC-F2	48.7	157.4	0.34
UHSC-F3	44.3	190.1	0.49
UHSC-F2-R5	37.8	147.4	0.55
UHSC-F3-R5	39.7	172.0	0.53

is about 2 times stronger than HSC. Additionally before the compressive strength is reached, the mechanical behavior of UHSC exhibits linear-elastic behavior. However, after the stress has reached the peak value, rupture occurs immediately under insufficient of load frame stiffeners. Specimens with added steel fibers (UHSC-F1, UHSC-F2, and UHSC-F3) exhibit an increased bridging effect associated with the toughness of the specimen, and an increase in toughness that is directly proportional to the volume fraction of steel fibers.

4.2 Dynamic test results

Table 4 and Figs. 5-17 shows the dynamic mechanical property test results. Table 3 shows the experimental results of repeated impact testing. All tests are conducted under the condition that air pressure in the high-pressure steel bottle is < 2 kg/cm^2. Under this condition, the projectile speed is roughly 11.0 m/sec. The actual velocity of the impact lever after each impact, however, is still measured by the grating speed detection device and oscilloscope. For the HSC-F1 specimen, damage is generated by the first impact; Fig. 5 shows the fracture mode. Fig. 6 shows the stress-strain curve of the specimen under quasi-static and dynamic loadings. As concrete is a compound material made by mixing aggregate of different grades and cementing material, air in the mixing process forms pores inside specimens. Additionally, during the solidifying contraction process of the

Table 4 Summary of repeated impact test

Specimen No.	Quasi-static Compression Strength (MPa)	Specimen Size (mm)	Impact velocity* (m/s)	Incident Energy E_I (J)	Reflected Energy E_R (J)	Transmitted Energy E_T (J)	Energy Absorption E_S (J)	Energy Absorption Ratio (J/cm^3)
HSC-F1	109.5	ϕ50×98.8	10.7	424.4	96.1	106.6	221.7	1.14
HSC-F2	101.9	ϕ50×98.8	11.5	500.1	96.1	134.3	269.8	1.39
			10.7	417.2	157.3	38.75	221.2	1.14
UHSC-F1	139.7	ϕ50×98.5	10.9	435.1	74.7	159.8	200.6	1.04
			10.9	435.9	63.5	132.2	240.3	1.24
UHSC-F2	157.4	ϕ50×97.5	10.8	429.0	58.6	244.5	125.9	0.66
			10.6	408.9	45.4	276.8	86.7	0.45
			10.4	401.8	48.5	290.3	63.1	0.33
			10.7	416.5	54.4	280.3	81.8	0.43
			4.9**	87.3	26.9	32.3	28.1	0.15
UHSC-F3	190.1	ϕ50×97.9	10.8	434.2	58.5	181.5	194.3	1.01
			10.9	443.0	54.6	312.3	76.2	0.40
			10.7	419.5	51.2	255.9	112.4	0.59
			10.8	430.8	56.8	287.2	86.8	0.45
			10.6	419.2	54.6	233.4	131.3	0.68

Note: *The pressure of the high-pressure steel bottle is kept under 2 kg/cm^2. Velocity of the projectile measured by the grating velocity detection device.
**Triggered when the aeration is incomplete.

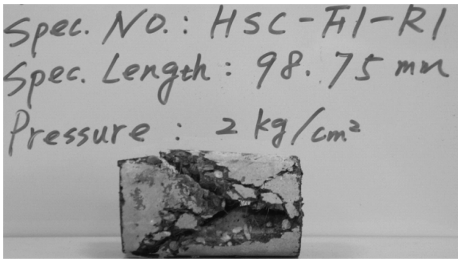

Fig. 5 Fracture mode of HSC-F1 specimen after one impact

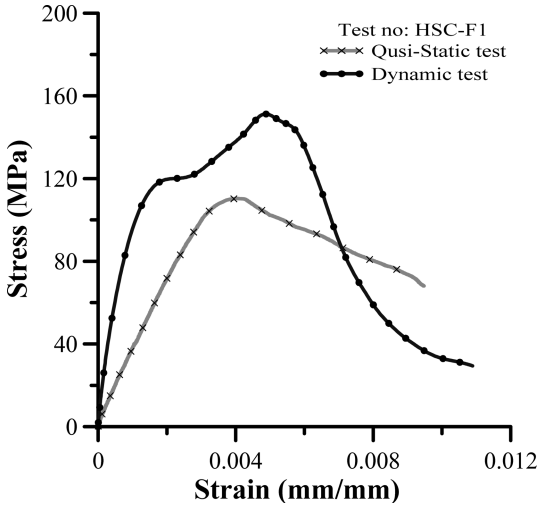

Fig. 6 Stress-strain curve of HSC-F1 specimen under quasi-static and dynamic loadings

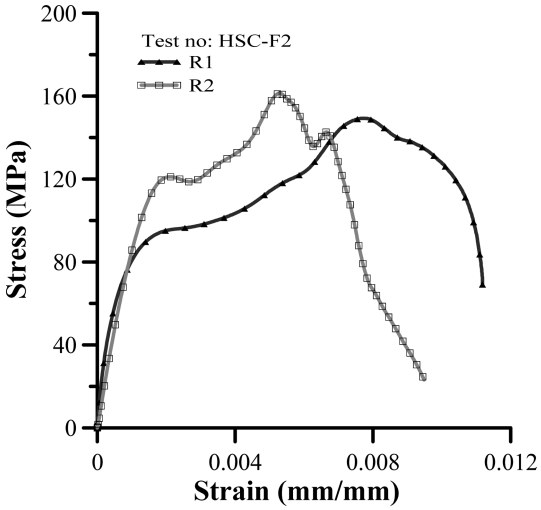

Fig. 7 Stress-strain curve of HSC-F2 specimen under repeated impact

concrete, contraction of the aggregate and cementing material differ. Consequently, a weakened transitional phase exists in the interface. A large number of micro cracks also exist in the area, resulting in microscopic heterogeneity of the material. The fracture process, therefore, can be considered the outcome of the combined effect of strain rate hardening (enhancing compressive strength and reducing corresponding strain) and damage softening. In the initial loading stage, damage is less significant than that during additional loading, and the major response is from the effect of strain-rate hardening. The compressive strength and initial elastic modulus increased from the quasi-static state (Fig. 6). As loading increases, material internal damage increases. When no steel-fiber is in a specimen or when volume fractions of the steel fibers are relatively low, a large number of micro cracks extend along the weakness band and form a damage transition zone, eventually resulting in specimen fracture.

Fig. 7 shows the stress-strain relationship of the HSC-F2 specimen under two repeated impacts. Since the bridging effect of the steel fiber increases stress, the decline in residual strength of the specimen slows, reflecting the toughness of steel-fiber concrete. The same specimen was destroyed by the second impact. A comparison of the experimental results of the two impact tests indicates that the stress of the second impact is greater than that of the first impact, primarily because action

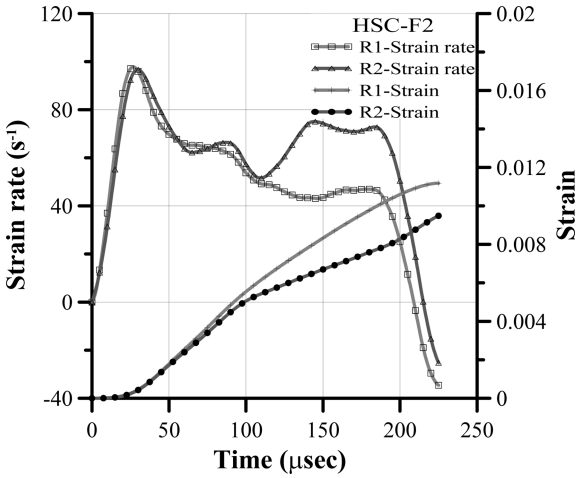

Fig. 8 Strain rate and strain history of HSC-F2 specimen after two repeated impacts

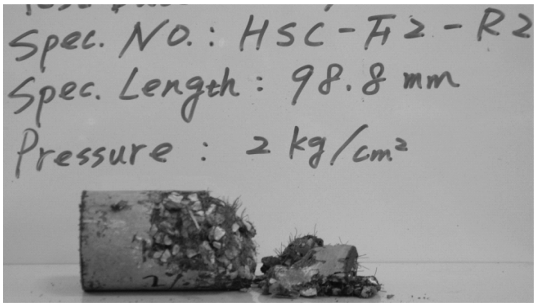

Fig. 9 HSC-F2 specimen after two impacts

time of the rectangular wave of the impact is two times the striker bar— is 195 μsec. According to the strain rate over time for the specimen subjected to two repeated impacts (Fig. 8), maximum strain ($\dot{\varepsilon} = 0$) of the specimen occurs when stress peaks at about 215 μsec, indicating that after loading is removed, deformation continues and then the compressed part bounces back. Following the second impact, increased peak stress is mainly due to strain rate hardening. According to the study by Bischoff and Perry (1995), compressive damage of concrete results from development of unstable micro cracks. When loading speed is high, inertial resistance is increased by the bridging effect, and cracking speed peaks or the steel fiber crosses both sides of the cracks, resulting in delayed deformation and increased dynamic strength during loading. This phenomenon can be seen from the strain over time (Fig. 8). Fig. 9 shows the fracture mode. Fig. 10 shows the stress-strain curve of the UHSC-F1 specimen after two repeated impacts. Its overall reaction trend resembles that of the HSC-F2 specimen. Fig. 11 shows the fracture mode of UHSC-F1 specimen.

Figs. 12 and 13 show stress-strain curves of the UHSC-F2 and UHSC-F3 specimens under repeated impacts, respectively. Compare the peak values of UHSC-F3 curves (Fig. 13), under the first impact, lower than those of UHSC-F2 (Fig. 12) and UHSC-F1 (Fig. 10). According to the one-dimensional wave propagation theory, the material's stress was calculated by output bar's strain signals. Owing to the UHSC-F3 with higher steel fiber volume fractions, cause more small holes

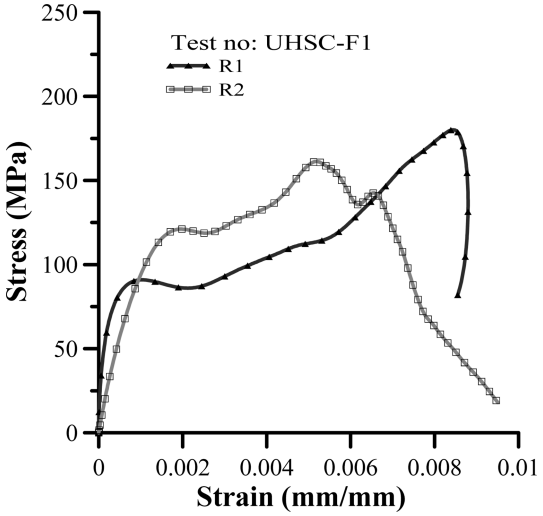

Fig. 10 Stress-strain curve of UHSC-F1 specimen under repeated impacts

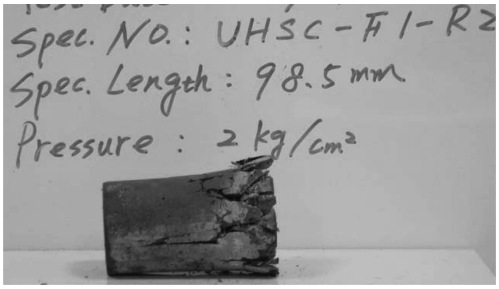

Fig. 11 UHSC-F1 specimen after two impacts

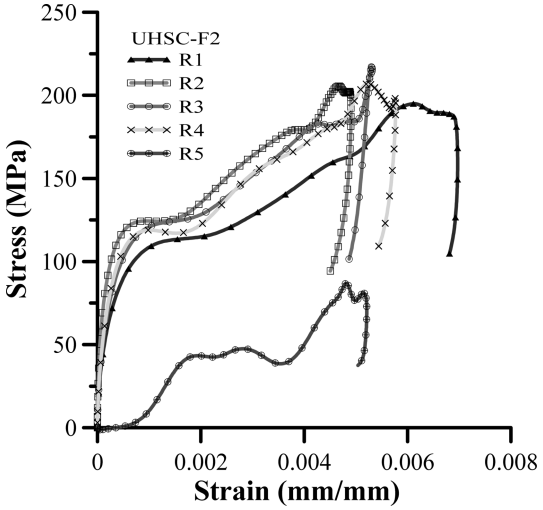

Fig. 12 Stress-strain curve of UHSC-F2 specimen under repeated impact

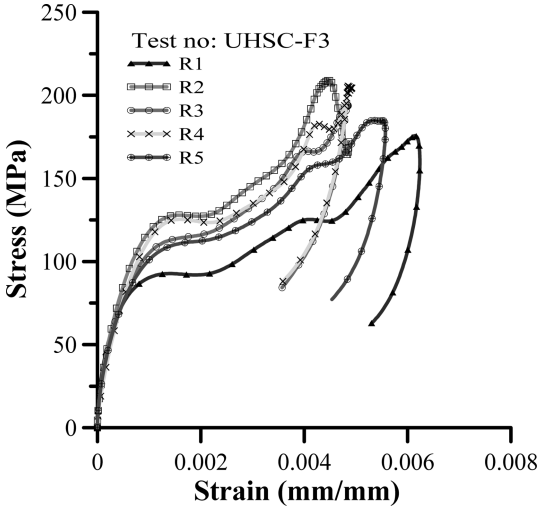

Fig. 13 Stress-strain curve of UHSC-F3 specimen under repeated impact

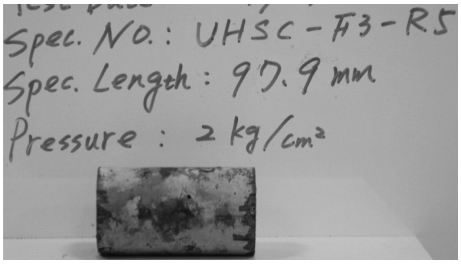

Fig. 14 UHSC-F3 specimen after five repeated impacts

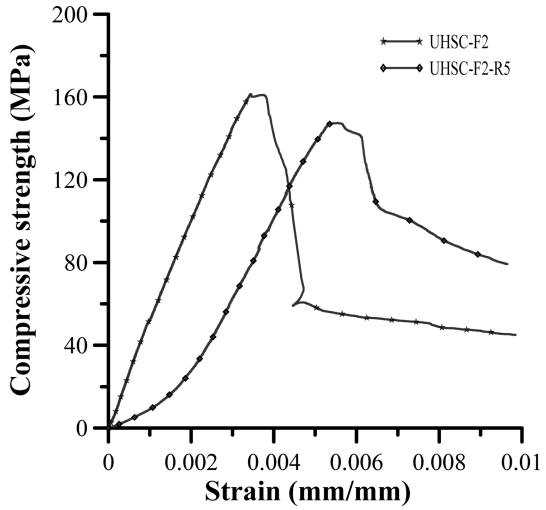

Fig. 15 Comparison of mechanical properties of UHSC-F2 specimen before and after impact

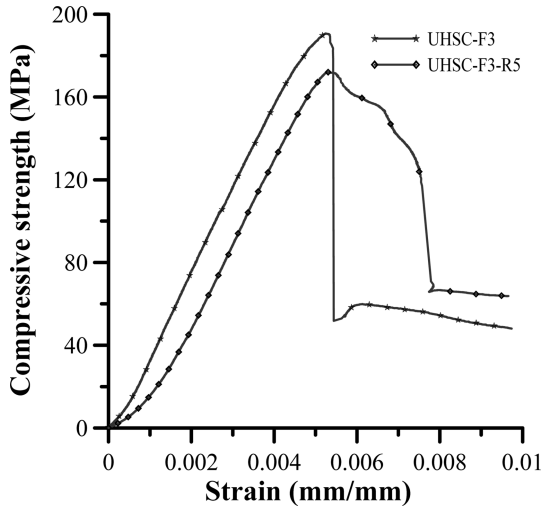

Fig. 16 Comparison of mechanical properties of UHSC-F3 specimen before and after impact

existing in the interior of the concrete, therefore, the impedance lower than UHSC-F2 and UHSC-F1. Under the first impact, the peak values lower than those. The responses of these two specimens (UHSC-F2 and UHSC-F3) are identical; that is, stress under the first impact is smaller than that of the second impact, and subsequence impact, the strength gradually decreases under ensuing reaction as the number of impacts increases. However, as the quasi-static compressive strength of these two specimens is higher than that of other specimens, and the fiber volume fractions of specimens are 2% and 3%, respectively, the bridging effect of steel fibers significantly increases binding stress. Therefore, under such a stress wave, the UHSC-F3 specimen shows no obvious damage (Fig. 14). Furthermore, the slopes (dynamic elastic modulus) of initial loading of sections of the UHSC-F3 specimen under five repeated impacts are relatively consistent.

To quantify the internal damage of the two sets of specimens under this condition, this study tests the two sets of specimens following impact with a MTS-810 100 ton servo hydraulic machine. This test uses the same displacement control as that used in the quasi-static experiment, and has a loading speed of 0.05 mm/min. Experiment findings demonstrate that the elastic modulus of the UHSC-F2 specimen remains 37.8 GPa, and compressive strength is 147.4 MPa; the elastic coefficient of the UHSC-F3 specimen remains 39.7GPa, and compressive strength is 172.0 MPa.

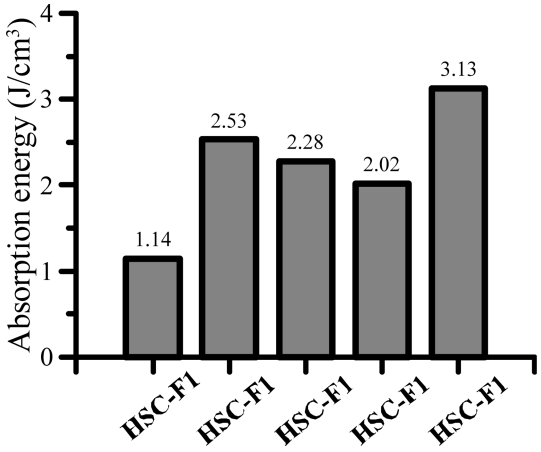

Fig. 17 Energy absorption of different specimens under repeated impacts

When the damage parameter is defined as $D = 1 - E_c/E_0$, where E_c and E_0 are post-stiffness declining elastic modulus and initial elastic modulus, respectively, the damage parameters for the UHSC-F2 and UHSC-F3 specimens are 0.23 and 0.10 respectively. Figs. 15 and 16 show the stress-strain curve changes of the two sets of specimens, respectively. Fig. 17 shows the energy absorption per unit volume of all specimens accumulated during the impact process. Experimental results suggest that energy absorption of the UHSC-F3 specimen is 3.13 J/cm^3, which is markedly superior to that of other specimens.

5. Conclusions

Based on repeated impact tests of HSC and UHSC of this study, we conclude the following:

1. This study performed repeated impact tests for specimens with various steel-fiber volume rates using a SHPB test device. Experimental findings indicate that when a specimen is under dynamic loading, the destruction process can be considered the result of the combined effect of strain rate hardening and damage softening. During the initial loading stage, damage is less significant than that during subsequent loading, and the major reaction is due to the effect of strain rate hardening. As loading increases, material internal damage increases. When a specimen had no steel fibers or when the volume of steel fibers was relatively low, a large number of micro cracks extended along the weakness band, forming a damage transition zone, and eventually resulting in specimen destruction.
2. Compressive damage of concrete results from development of unstable micro cracks. When loading speed is high, the increase in inertial resistance is caused by the bridging effect and the fact that cracking speed peaks or steel fibers crossing both sides of the cracks, resulting in delayed deformation and an increase in dynamic strength during loading.
3. Under impact loadings, the dynamic energy absorption property of specimens is directly proportional to specimen strength and steel-fiber content. Experimental results suggest that the energy absorption of the UHSC-F3 specimen is markedly superior to that of other specimens.

References

ACI Committee 363 Report (1984), *ACI Mater. J.*

Banthia, N., Mindess, S. and Trottier, J.F. (1996), "Impact resistance of steel fiber reinforced concrete", *ACI Mater. J.*, **93**(5), 472-479.

Banthia, N., Yan, C. and Sakai, K. (1998), "Impact resistance of fiber reinforced concrete at subnorma temperatures", *Cement Concrete Compos*., **20**(5), 393-404.

Bindiganavile, V. and Banthia, N. (2005), "Impact response of the fiber-matrix bond in concrete", *Can. J. Civil Eng*., **32**(5), 924-933.

Bischoff, P.H. and Perry, S.H. (1995), "Impact behavior of plain concrete loaded in uniaxial compression", *J. Eng. Mech.*, **121**, 685-693.

Dancygier, A.N. and Yankelevsky, D.Z. (1996), "High strength concrete response to hard projectile impact", *Int. J. Impact Eng*., **18**(6), 583-599.

Dancygier, A.N. and Yankelevsky, D.Z. (1999), "Effects of reinforced concrete properties on resistance to hard projectile impact", *ACI Struct. J*., **96**(2), 259-267.

Deng, Z.C. and Li, J.H. (2007), "Tension and impact behaviors of new type fiber reinforced concrete", *Comput. Concrete,* **4**(1), 19-32.

Gong, J.C., Malvern, L.E. and Jenkins, D.A. (1990), "Dispersion investigation in the split Hopkinson pressure bar", *J. Eng. Mater-T. ASME,* **112**, 309-314.

Hackman, L.E., Farrell, M.B. and Dunham, O.O. (1992), "Slurry infiltrated mat concrete (SIMCON)", *Concrete Int., Des. Construct.*, **14**(12), 52-56.

Hanchak, S.J., Forrestal, M.J., Young, E.R. and Ehrgott, J.Q. (1992), "Perforation of concrete slabs with 48 MPa(7 ksi) and 140 MPa(20 ksi) unconfined compressive strengths", *Int. J. Impact Eng*., **12**(1), 1-7.

Kolsky, H. (1949), "An investigation of the mechanical properties of materials at very high rates of loading", *Proc. Phys. Soc*., **B62**, 676-700.

Lankard, D.R. (1985), "Slurry infiltrated fiber concrete (SIFCON): properties and applications", *Proceedings of Symposium on Very High Strength Based Materials*, Materials Research Society, Pittsburgh.

Richard, P. and Cheyrezy, M. (1995), "Composition of reactive powder concretes", *Cement Concrete Res.,* **25**(7), 1501-1511.

Ross, C.A., Tedesco, J.W. and Kuennen, S.T. (1995), "Effects of strain rate on concrete strength", *ACI Mater. J*., **92**(1), 37-47.

Smadi, M.M. and Belakhdar, K.A. (2007), "Nonlinear finite element analysis of high strength concrete slabs", *Comput. Concrete,* **4**(3), 187-206.

Tai, Y.S. (2009), "Flat ended projectile penetrating ultra-high strength concrete plate target", *Theor. Appl. Fract. Mec*., **51**, 117-128.

Tang, T., Malvern, L.E. and Jenkins, D.A. (1991) "Rate effects in uniaxial dynamic compression of concrete", *J. Eng. Mech.*, **118**(1), 108-124.

Teng, T.L., Chu, Y.A., Chang, F.A. and Chin, H.S. (2004), "Calculating the elastic moduli of steel-fiber reinforced concrete using a dedicated empirical formula", *Comput. Mater. Sci*., **31**(3), 337-346.

Wang, Z.L., Liu, Y.S. and Shen, R.F. (2008), "Stress-strain relationship of steel fiber-reinforced concrete under dynamic compression", *Constr. Build. Mater*., **22**(5), 811-819.

Zhang, G., Liu, B., Bai, G. and Liu, J. (2009), "Experimental study on seismic behavior of high strength reinforced concrete frame columns with high axial compression ratios", *Struct. Eng. Mech.*, **33**(5), 653-656.

Zhang, M.H., Shim, V.P.W., Lu, G. and Chew, C.W. (2005), "Resistance of high-strength concrete to projectile impact", *Int. J. Impact Eng*., **31**(7), 825-841.